


**Interplay of elastic instabilities and viscoelasticity in the finite deformation of thin membranes**

Eduard Benet, Hongtian Zhu, and Franck J. Vernerey\*

*Department of Mechanical Engineering, University of Colorado at Boulder, Boulder, Colorado 80309, USA* (Received 18 November 2018; revised manuscript received 17 February 2019; published 17 April 2019)

Pneumatic structures and actuators are found in a variety of natural and engineered systems such as dielectric actuators, soft robots, plants and fungi cells, or even the vocal sac of frogs. These structures are often subjected to mechanical instabilities arising from the thinning of their cross section and that may be harvested to perform mechanical work at a low energetic cost. While most of our understanding of this unstable behavior is for purely elastic membranes, real materials including lipid bilayers, elastomers, and connective tissues typically display a time-dependent viscoelastic response. This paper thus explores the role of viscous effects on the nature of this elastic instability when such membranes are dynamically inflated. For this, we first introduce an extension of the transient network theory to describe the finite strain viscoelastic response of membranes, enabling an elegant formulation while keeping a close connection with the dynamics of the underlying polymer network. We then combine experiments and simulations to analyze the viscoelastic behavior of an inflated blister made of a commercial adhesive tape (VHB 4905). Our results show that the viscous component induces a rich spectrum of behaviors bounded by two well-known elastic solutions corresponding to very high and very low inflation rates. We also show that membrane relaxation may induce unwanted buckling when it is subjected to cyclic inflations at certain frequencies. These results have clear implications for the inflation and mechanical work performed by time-dependent pneumatic structures and instability-based actuators.

DOI: [10.1103/PhysRevE.99.042502](https://doi.org/10.1103/PhysRevE.99.042502)**I. INTRODUCTION**

Pneumatic structures and actuators based on the inflation of thin membranes are an important component of many industrial and natural systems, such as the vocal sac of frogs [1], soft robots [2], or baromorphs [3]. Despite the variety in their nature and composition, these membranes are characterized by their capability to undergo extremely large strains (>100%), and the fact that they often exhibit a strong viscoelastic response [4]. Due to their large distortions, membranes often display mechanical instabilities. For example, the thinning of a stretched rubber membrane affects its internal pressure [5] and the electric field across it [6]. Surface wrinkles appear due to a competition between curvature and compressive strains [7], and cellular blebbing [8] is caused by a competition between adhesion and internal pressure. These and other instabilities are the keys to understanding the mechanics of greater problems such as the vesicle transport in porous media [9,10] or the electroporation in animal cells [11]. In addition, many technological applications are designed to harvest those instabilities and use them in actuators [12], energy harvesting [13], or even medical applications [14] at low energetic cost. However, while there is extensive literature devoted to understanding the physics behind these instabilities in the elastic regime, the role of viscosity is still poorly understood. To the best of our knowledge, the interplay between elastic instability and viscous relaxation has only been reported in the context of dielectric elastomers,

where several authors stressed the importance of how viscous effects delay, stabilize, or even eliminate these instabilities [15–17].

Viscoelasticity in highly deformable shells is often approached from the perspective of fluidlike thin films in which the shell or membrane is modeled using a creeping flow [18]. This is the case of thin viscous sheets such as syrup [19], but the same approach is also used in the broader context of biomembranes [20–23] due to their faster relaxation times with respect to other simultaneous processes [24–26]. Regarding solidlike materials such as polymers [27], researchers have relied on coupling shell theory with known constitutive equations for viscoelasticity such as the standard linear solid [28], K-BKZ [29], Christensen [30,31], or CBT [32] models. These approaches are phenomenological and thus provide little information on the molecular mechanisms driving these behaviors [33,34]. In this sense, the transient network theory (TNT) [35,36] enables us to obtain a statistical knowledge of the molecular processes leading to viscoelasticity in active networks [37,38] and is often used to investigate the physics behind non-Newtonian fluids [39] and the solid-fluid transition. Taken in the context of shells and membranes, it might, therefore, impact our understanding of lipids mono- and bilayers [40], viscous sheets [41], or polymeric membranes.

In this paper, we concentrate on using this statistical approach to study the interactions between large elastic deformation and viscous relaxation during the common snap-through [42] instability of rubber membranes. We first present a series of experimental results on a commercial viscoelastic adhesive tape (VHB 4905) that illustrate the role of relaxation at the onset and the extent of mechanical instabilities (due

\*franck.vernerey@colorado.edu;  
<https://www.colorado.edu/lab/vernerey>

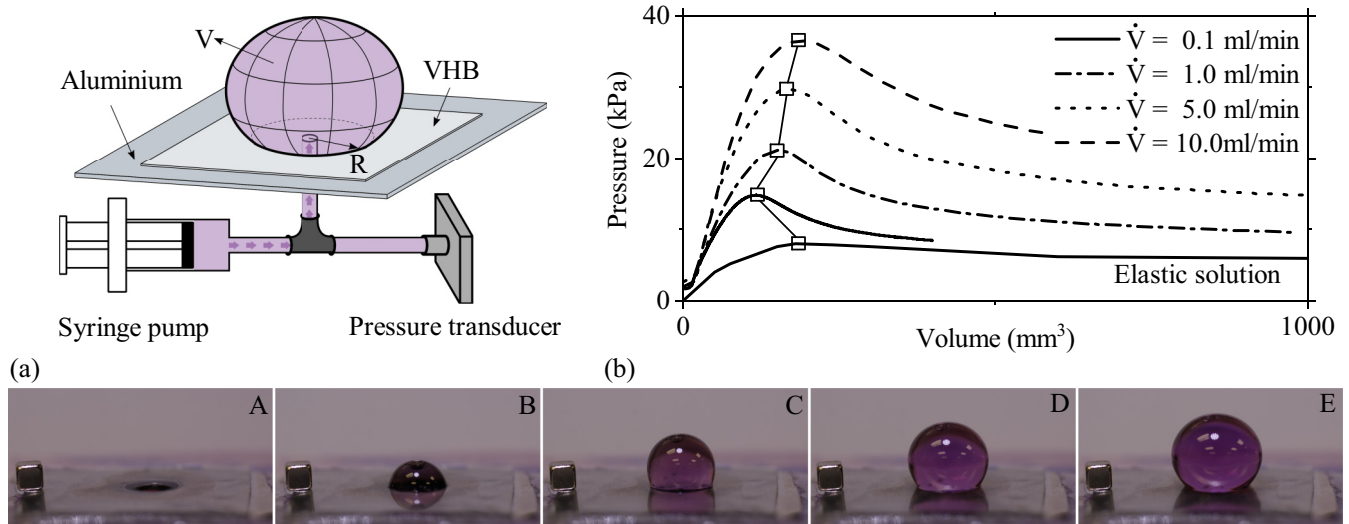


FIG. 1. (a) Scheme of the blister inflation experimental setup. (b) Experimental results on the internal blister pressure vs the internal fluid volume obtained at four different inflation speeds:  $\dot{V} = 0.1, 1, 5,$  and  $10$  mL/min. The insets A–E are actual snapshots of the experiment at five different stages ranging from  $V = 0$  to  $400$  mL. The reference cube has a  $3.5$  mm edge.

to membrane thinning and buckling). After deriving the TNT for membranes, we then explore the observed blister response in the case of constant inflation rates and cyclic loading. Model results not only provide a good interpretation of experimental results, but they also predict how the competition between loading rate and relaxation time drives the nature of instabilities.

## II. EXPERIMENTAL GROWTH OF VISCOELASTIC BLISTERS

Our experiment consists of inflating a blister under a viscoelastic adhesive tape (VHB 4905) firmly attached to an aluminum substrate through a central hole of radius  $R$  [Fig. 1(a)]. The inflation process is driven by an NE-1000 syringe pump (NEWERA Pump Systems, Inc.) that injects dyed water at a controllable volume rate  $\dot{V}$  using a network of polyethylene tubing. In parallel, a pressure transducer (Omega PX26-005GV) connected to a DAQ system (NI-9211 and NI USB-9162) and powered with a dc power source allows constant monitoring of the pressure with precision between 0 and 5 psi. To prevent the delamination of the material during inflation, the neck of the blister is firmly constrained at all times such that we obtain the blister growth depicted in the insets A–E in Fig. 1. Three parameters, therefore, control the system: the volume inflation rate  $\dot{V}$ , the initial tape thickness  $h_0$ , and the initial blister neck radius  $R$  [Fig. 1(a)]. Due to the known viscous response of the material [43], the initial results are presented in the form of pressure-volume curves for a blister with parameters  $R = 3.5$  mm,  $h_0 = 0.5$  mm, and various inflation rates ( $\dot{V} = 0.001$ – $10$  mL/min) [Fig. 1(b)]. In addition, these results are compared to an elastic solution that we obtained via quasistatic inflation. For this, we inflated multiple blisters to different volumes and allowed them to relax for large periods of time ( $>10$  h) until the pressure reached a steady state. The different pressure-volume points

obtained with this method were combined to obtain the bottom curve of Fig. 1(b), which we labeled as an elastic solution. Each of these curves shows a nonlinear relationship between pressure and volume, which we characterize by two measures: (i) the magnitude of the maximum or critical pressure, and (ii) the critical volume at which this instability occurs. In the case of an elastic membrane ( $\dot{V} \rightarrow 0$ ), this instability is known to result from the thinning of the rubber membrane at large strains and a subsequent drop in internal pressure [5]. We show here that a similar phenomenon also occurs for larger inflation rates where viscous effects become dominant. In particular, it can be seen that while the critical pressure increases monotonically with the inflation rate, the critical volume first shows a drop and then a rise with the inflation rate. In theory, this critical volume should be the same at very slow and very fast inflations as they both correspond to different scalings of the elastic solution.

It is clear that this time-dependent behavior can drastically affect the behavior of blisters subjected to dynamic and cyclic loading. To illustrate this point, we subjected the blister to a single inflation-deflation cycle (up to a volume of  $0.7$  mL) at two different speeds: a fast process driven at  $\dot{V} = 0.1$  mL/s and a slower one driven at  $\dot{V} = 0.004$  mL/s. The blister was then deflated at the same speed until it buckled, and finally it was left to relax until it recovered a smooth shape. As shown in Fig. 2, the blisters display a very different buckling-recovery pattern depending on the inflation rate. For slow inflation [Fig. 2(b)], buckling appears at a high volume, and the blister takes a long time to recover a quasispherical shape. For fast inflation, however [Fig. 2(a)], the blister buckles at a small volume, and relaxation occurs almost instantaneously. To understand these puzzling behaviors, we first introduce a model to capture the viscoelasticity of a membrane at large strains based on the transient network theory (TNT) and then we explore the problem of rate-dependent blister inflation.

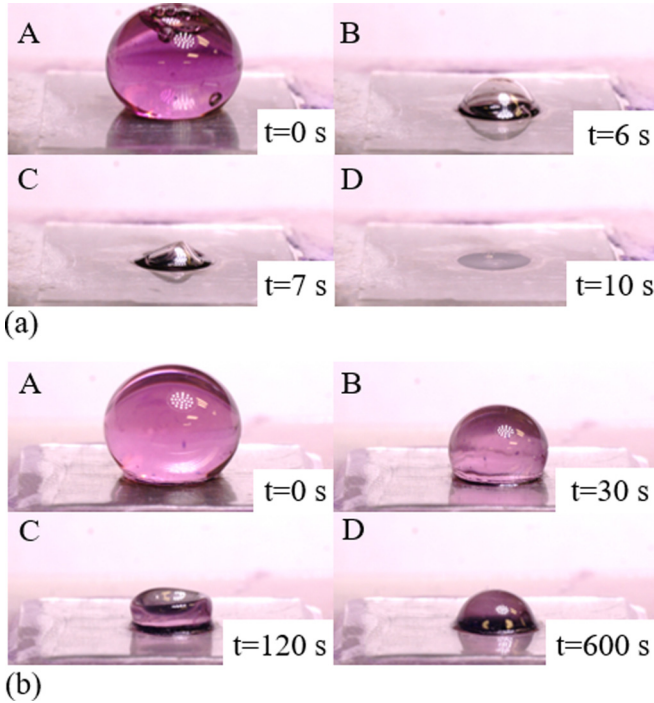


FIG. 2. (a) Deflation cycle performed of a slowly inflated blister made of VHB 4905 with initial radius  $R = 3.5$  mm. The images show the maximum inflation at 700 mL (A), the shape prior to buckling (B), buckling (C), and the final relaxed state (D). (b) Same as (a) using an extremely fast inflation-deflation speed.

### III. TRANSIENT NETWORK THEORY FOR THIN MEMBRANES

The theory of thin membranes [44] idealizes a thin layer as a two-dimensional surface embedded in a three-dimensional space. Due to the membrane's small thickness, two main assumptions can usually be made: (a) bending moments are negligible compared to in-plane stresses, and (b) the normal vector  $\mathbf{n}$  at any point remains normal during deformation. The latter implies that we can parametrize the membrane by two in-plane coordinates  $\xi^\alpha$  ( $\alpha = 1, 2$ ) and one out-of-plane coordinate  $\xi$  such that the position  $\mathbf{x}$  of a point in the

membrane is

$$\mathbf{x} = \boldsymbol{\varphi}(\xi^\alpha) + \xi \nu \mathbf{n}, \quad \xi \in \left[ -\frac{h_0}{2}, \frac{h_0}{2} \right], \quad (1)$$

where  $\boldsymbol{\varphi}(\xi^1, \xi^2)$  is the coordinate on the midplane while  $\nu$  is the ratio between the current  $h$  and reference thickness  $h_0$ . In the remainder of the paper, we use  $\alpha$  to indicate the two tangent coordinates, and the index 3 to indicate the normal direction. Furthermore, instead of precise but more complex index notation, we prefer here to use a more generic tensor notation for clarity. Details regarding the component form of the presented equations are provided in Appendix A for the interested reader. Following [44], the stress state of a membrane is characterized by the in-plane Cauchy stress tensor  $\boldsymbol{\sigma}$ , which is obtained by integrating the Cauchy stresses over the thickness of the shell. This tensor has nonzero components  $\sigma^{\alpha\beta}$  that are proportional to the membrane thickness  $h$  (Fig. 3), and whose dimensions are of line tension (force per length). Considering then a membrane with external pressures applied tangential  $f^\alpha$  and normal  $f^3$  to the midplane, the balance of linear momentum takes the form [45]

$$\sigma^{\alpha\beta}{}_{|\beta} + f^\alpha = 0, \quad \sigma^{\alpha\beta} \kappa_{\alpha\beta} + f^3 = 0, \quad (2)$$

where the vertical bar in the first equation indicates a covariant derivative, and  $\kappa_{\alpha\beta}$  is the curvature tensor (or second fundamental form) of the surface (see Appendix A for details). Despite their apparent complexity, one can easily interpret the physical meaning of these equations by drawing an analogy with the Laplace law in fluid interfaces. Indeed, the second of Eqs. (2) establishes that the pressure applied normally to the membrane is balanced by the surface tension  $\sigma^{\alpha\beta}$  times the curvature  $\kappa_{\alpha\beta}$  at that particular point.

The viscoelastic response of polymers arises from a variety of molecular dynamics including molecular entanglements [46], dynamic bonds [47], or diffusion of molecular chains [48], among others. When these dissipative mechanisms are coupled with large elastic deformations, we have previously shown that the TNT [49] provides a convenient mathematical description. With this approach, a polymer is conceptualized as  $N + 1$  interpenetrated and independent networks of cross-linked molecular chains (Fig. 3). These networks can belong to two categories: (a) dynamic networks are those

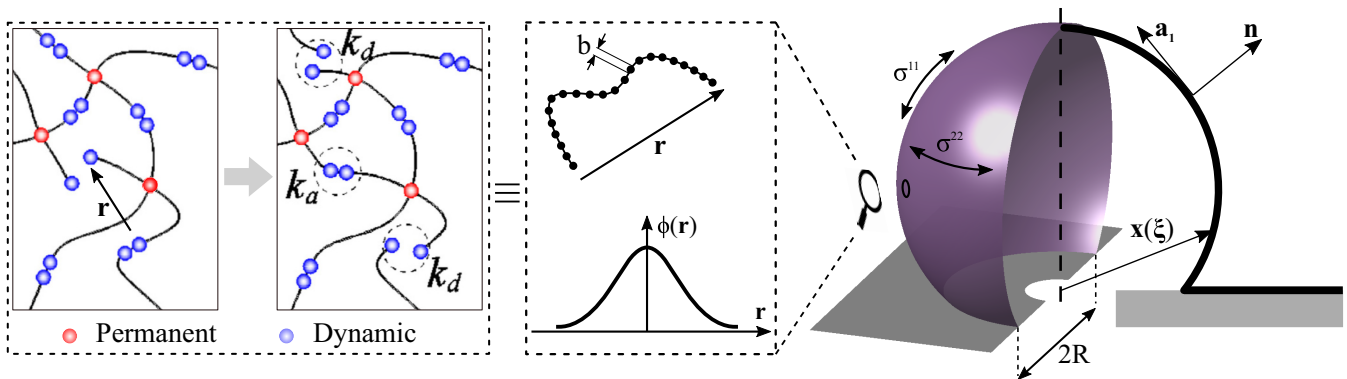


FIG. 3. Scheme of the parametrization  $\mathbf{x}$  of an axisymmetric blister with neck radius  $2R$ , local basis  $\mathbf{a}_1, \mathbf{n}$ , and principal stresses  $\sigma^{11}, \sigma^{22}$ . The inset on top represents a scheme of a polymer made of a combination of permanent and dynamic bonds with attachment and detachment rates  $k_a$  and  $k_d$ , respectively.

in which cross-links constantly attach and detach at rates  $k_a$  and  $k_d$ , respectively, and thus provide a viscous component to the material; (b) permanent networks have permanent (or covalent) cross-links ( $k_a = k_d = 0$ ) and thus provide an elastic response. In this study, the elastic network is denoted by the index 0, while the dynamic networks are denoted by indices  $n = 1$  to  $N$ . To derive a constitutive relation based on these assumptions, a molecular chain is idealized as the collection of  $\mathcal{N}$  Kuhn segments of length  $b$ , and characterized by its end-to-end vector  $\mathbf{r}$  (Fig. 3). The mechanics of the  $n$ th network may then be understood through the distribution  $\phi_n$  (Fig. 3) of this end-to-end vector  $\mathbf{r}$  within a continuum point. Following [36], a domain  $\Omega$  made of a population of polymer chains with total concentration  $C_n$  can then be characterized by two key quantities: the concentration  $c_n$  of attached chains (i.e., those that are connected to the network and contribute to the mechanical response) and the chain distribution tensor  $\boldsymbol{\mu}_n$ :

$$c_n = \int_{\Omega} \phi_n(\mathbf{r}) d\Omega, \quad \boldsymbol{\mu}_n = \frac{3}{c\mathcal{N}b^2} \int_{\Omega} \phi_n(\mathbf{r}) \mathbf{r} \otimes \mathbf{r} d\Omega. \quad (3)$$

From its definition, it can be inferred that  $\boldsymbol{\mu}_n$  represents mean-squared stretch experienced by attached chains in the  $n$ th network; it is directly related to the stored elastic energy and internal stress in the corresponding network. Following [36], the Cauchy stress tensor in the polymer follows an additive decomposition, which in the case of a membrane we can write as

$$\boldsymbol{\sigma} = h \left( \sum_{n=0}^N c_n k_B T (\boldsymbol{\mu}_n - \mathbf{I}) + p \mathbf{I} \right), \quad (4)$$

where  $k_B T$  is the thermal energy of a single polymer chain,  $\mathbf{I}$  is the identity tensor, and  $p$  is the internal pressure, which acts as a Lagrange multiplier enforcing the material's incompressibility. We note that the term  $c_n k_B T$  has units of force per unit length and it corresponds to the shear modulus  $G_n$  of each individual network [36]. For a thin membrane, this expression can be simplified by noting that  $\sigma^{33} = 0$ . Indeed, if we consider the normal component of the distribution tensor as  $\mu_n^t = \mathbf{n} \cdot \boldsymbol{\mu}_n \cdot \mathbf{n}$ , the internal pressure is then determined as  $p = \sum G_n (1 - \mu_n^t)$ . By substituting this result into  $\boldsymbol{\sigma}$  and integrating over the thickness, we obtain a universal constitutive equation for the viscoelastic stress in membranes as

$$\boldsymbol{\sigma} = \sum_{n=0}^N h G_n (\boldsymbol{\mu}_n - \mu_n^t \mathbf{I}). \quad (5)$$

It can easily be shown that the pure elastic case ( $n = 0$ ) converges to a neo-Hookean elastic model with shear modulus  $G_0 = c_0 k_B T$  [36]. The stress can therefore be additively decomposed into a purely elastic component  $h G_0 (\boldsymbol{\mu}_0 - \mu_0^t \mathbf{I})$  and  $N$  viscoelastic contributions.

The problem is then reduced to determining the evolution of the concentrations  $c_n$  of attached chains and their distribution  $\boldsymbol{\mu}_n$  over time. We have previously shown [36] that general evolution equations for these quantities follow

first-order kinetics as follows:

$$\dot{c}_n = k_a (C_n - c_n) - k_d c_n, \quad (6a)$$

$$\dot{\boldsymbol{\mu}}_n = k_a \frac{(C_n - c_n)}{c_n} \mathbf{I} - k_d \boldsymbol{\mu}_n + \mathbf{L} \boldsymbol{\mu}_n + \boldsymbol{\mu}_n \mathbf{L}^T, \quad (6b)$$

where  $\mathbf{L}$  is the velocity gradient. We see here that the evolution of chain stretch in networks is driven by their attachment in their natural state at a rate  $k_a$ , their detachment in their current state at a rate  $k_d$ , and finally their elastic distortion due to an imposed rate of deformation, represented by the velocity gradient  $\mathbf{L}$ . We finally note that this model simplifies if the rates  $k_a$  and  $k_d$  are independent of chain deformation. In these cases, (6a) and (6b) are decoupled, and the concentration  $c_n$  quickly reaches a steady state given by  $c_n = C_n k_a / (k_a + k_d)$ . Substituting this result in (6b) leads to

$$\dot{\boldsymbol{\mu}}_n = -k_d (\boldsymbol{\mu}_n - \mathbf{I}) + \mathbf{L} \boldsymbol{\mu}_n + \boldsymbol{\mu}_n \mathbf{L}^T. \quad (7)$$

Furthermore, if one expresses this equation in the curvilinear coordinate system  $(\mathbf{a}_1, \mathbf{a}_2, \mathbf{a}_3)$ , where  $\mathbf{a}_i = \frac{\partial \mathbf{x}}{\partial \xi^i}$  (see Appendix A for details), the evolution of the tensor  $\boldsymbol{\mu} = \mu^{ij} \mathbf{a}_i \otimes \mathbf{a}_j$  becomes

$$\dot{\boldsymbol{\mu}}_n = \dot{\mu}_n^{ij} \mathbf{a}_i \otimes \mathbf{a}_j + \mu_n^{ij} \dot{\mathbf{a}}_i \otimes \mathbf{a}_j + \mu_n^{ij} \mathbf{a}_i \otimes \dot{\mathbf{a}}_j. \quad (8)$$

All three terms on the right-hand side can be readily identified with those appearing in Eq. (7). In other words, in this appropriate curvilinear system, the evolution of the distribution tensor degenerates to the simple component equation

$$\dot{\mu}_n^{ij} = -k_d (\mu_n^{ij} - a^{ij}). \quad (9)$$

The variations of the components of the distribution tensor are therefore related to the viscoelastic component of the stress, and one obviously has  $\dot{\mu}_0^{ij} = 0$ . In summary, the deformation of the membrane is defined by the combination of Eqs. (2), (5), (6a), and (6b).

#### IV. INFLATION OF VISCOELASTIC BLISTERS AT CONSTANT RATES

We explore here the behavior of a viscoelastic blister at constant inflation rates. We start by deriving an exact solution for a spherical membrane, which provides a good approximation of a blister undergoing large deformation. We then confirm our findings by exploring the more complex geometry of a real blister.

##### A. Solution for spherical viscoelastic membranes

To gain insight into our experimental results, we therefore consider first the inflation of a spherical membrane with an initial radius  $R_0$  and thickness  $h_0$  [Fig. 4(b)]. The elastic solution for this problem is well known in the literature [50,51] and is commonly used to illustrate elastic instabilities. However, to the best of our knowledge, although there are some viscoelastic versions of this problem [29], the effect of viscosity on the mechanical instability is still poorly understood. During spherical inflation, the membrane deformation is entirely defined by the change in radius  $R = \lambda R_0$ . Hence, a solution to this problem involves integrating the distribution tensor in time and use Eq. (2) to determine the internal

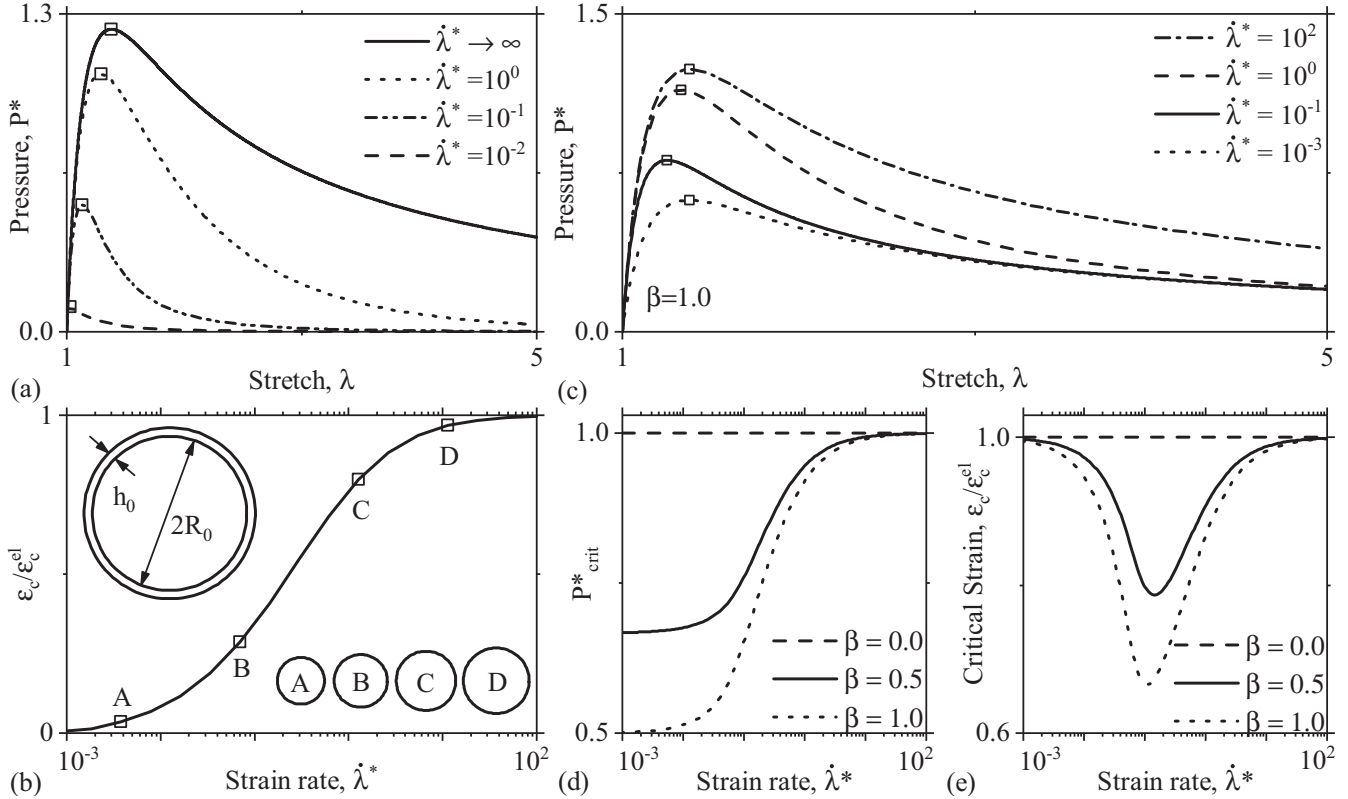


FIG. 4. (a) Normalized pressure  $P^*$  vs the radial strain  $\lambda = R/R_0$  during the inflation of a spherical membrane made of a single dynamic network  $c_1 = 0$ . (b) Evolution of the critical strain  $\epsilon_c/\epsilon_c^{el}$ , where the  $P^*$ - $\lambda$  diagram takes the maximum value. The insets represent a comparison between the minimum and the maximum relative size at which this maximum takes place. (c) Normalized pressure  $P^*$  vs the radial strain  $\lambda = R/R_0$  during the inflation of a spherical membrane with  $\beta = 1$ . (d) Variation of the maximum pressure in the (a) and (b) diagrams with the strain rate, and its comparison with the purely elastic case  $c_2 = 0$ . (e) Variation of the strain  $\lambda_c$  that gives the maximum pressure with the strain rate and its comparison with the elastic case  $c_2 = 0$ .

pressure  $P$  (details are provided in Appendix B). Regarding the constitutive equation, we choose here a simple approach in which the polymer is made of a permanent network with a constant  $c_0$  and a single dynamic network with constants  $c_1$  and  $k_d$ . Altogether, these assumptions lead to the following expression relating the radial strain  $\lambda$  to the internal pressure  $P$ :

$$P^* = 2c_0^*(\mu_0^\lambda - \mu_0^h) + 2c_1^*(\mu_1^\lambda - \mu_1^h), \quad (10)$$

where  $\mu_0^\lambda = 1/\lambda$ ,  $\mu_0^h = 1/\lambda^7$ , and

$$\mu_1^\lambda = \frac{1}{\lambda} e^{-k_d t} + \frac{k_d}{\lambda} \int_0^t \frac{e^{k_d(\zeta-t)}}{\lambda(\zeta)^2} d\zeta, \quad (11)$$

$$\mu_1^h = \frac{1}{\lambda^7} e^{-k_d t} + \frac{k_d}{\lambda^7} \int_0^t \lambda(\zeta)^4 e^{k_d(\zeta-t)} d\zeta. \quad (12)$$

This solution contains two contributions, weighted by  $c_0^*$  and  $c_1^*$ , respectively. The former corresponds to the elastic response of the permanent network, and it matches the classical result for the inflation of a spherical neo-Hookean membranes [52]. The latter corresponds to the viscous or rate-dependent contribution. For convenience, we normalize the problem based on the total number of attached bonds as  $c_n^* = \frac{c_n}{c_0+c_1}$  ( $n = 0, 1$ ) and  $P^* = PR_0/(\sum c_n k_B T h_0)$ , implying that the reference shear modulus is  $G = G_0 + G_1$ . Using this, let us

explore the behavior of a membrane made of a purely dynamic network ( $c_0^* = 0$ ) (that may be compared to a Maxwell model in its linearized form). In this case, the pressure takes the form

$$P^* = 2(\mu^\lambda - \mu^h). \quad (13)$$

We plot in Fig. 4(a) the variation of the normalized pressure  $P^*$  with radial stretch  $\lambda$  for different inflation rate  $\dot{\lambda}^* = \dot{\lambda}/k_d$ . We note that when inflated quickly ( $\dot{\lambda}^* \rightarrow \infty$ ), the sphere converges to a purely elastic membrane with shear modulus  $G = c_1 k_B T$  [Fig. 4(a)] and an elastic instability occurring at the classical critical stretch  $\lambda_c = 1.38$ . As the inflation rate decreases, however, the solution shifts the magnitude and position of this critical value until it eventually vanishes when the timescale of the inflation is smaller than the material relaxation. Interestingly, we observe a nontrivial shift of the coordinate  $[\lambda_c, P_c]$  of the critical point. On the one hand, we observe the expected decrease in critical pressure due to the stress relaxation on the membrane. This behavior, similar to that observed in the blister tests, is a direct result of the dynamic network, which acts as a viscous damper. On the other hand, Fig. 4(b) shows that the model predicts a nonlinear increase of the critical strain  $\epsilon_c = \lambda_c - 1$  with inflation rate  $\dot{\lambda}^*$ . This may be explained as follows: for very slow rates, the polymer behaves like a fluid and thus shows immediate relaxation  $\epsilon_c \approx 0$ . In contrast, as the inflation speed increases,

the membrane starts showing an elastic behavior and its associated instability at  $0 < \epsilon_c < 0.38$ . Finally, at large inflation rates, the membrane becomes quasielastic, and we recover the elastic solution  $\epsilon_c = 0.38$ .

Let us now consider the case in which both the permanent and dynamic networks are present [Eq. (10)]. For this, it is useful to separate the contribution from each network with the parameter  $\beta = c_1^*/c_0^*$ . Now, due to the presence of the permanent network, the  $P^*$ - $\lambda$  relationship converges to the same solution in both quasistatic and extremely fast inflations with a scale factor of  $(1 + \beta)$ . Indeed, the shear moduli corresponding to a relaxed and instantaneous inflation are, respectively,  $G_0 = c_0 k_B T$  and  $G_i = (1 + \beta)G_0$ . Furthermore, in the boundary  $\beta \rightarrow 0$ , the system converges to the quasistatic solution with modulus  $G_0$  regardless of the inflation speed. In intermediate cases, however, the elastic behavior of the permanent network coexists with the viscous dissipation of the dynamic one. In this case, the previous analysis on extremely slow and extremely fast inflation indicates that the position of  $\epsilon_c$  must remain unchanged at the inflation boundaries  $\dot{\lambda} \rightarrow 0$  and  $\dot{\lambda} \rightarrow \infty$  [Fig. 4(d)]. Regarding its magnitude, the critical pressure scales with  $(1 + \beta)$  between these two scenarios [Fig. 4(c)]. By plotting these two quantities [Figs. 4(b) and 4(c)], we observe a nonlinear variation where the critical strain is reduced on intermediate inflations, while the critical pressure always increases with the inflation rate. Indeed, as long as the viscous contribution is present, we observe the same shift to lower critical strains. However, this effect disappears as the contribution of the dynamic network vanishes ( $\lambda^* \rightarrow 0$ ) and we are left with a purely elastic membrane.

### B. Inflation of a viscoelastic blister

Using the general formulation, let us now concentrate on the problem of an axisymmetric blister with radius  $R$  being inflated at a rate  $\dot{V}$  (Fig. 3). The governing equations for this particular problem (see Appendix C) now consist of nonlinear partial differential equations that do not lend a simple solution. For this reason, we constructed a numerical solution by discretizing the strong form of Eq. (2) using the extended particle difference method [53,54], and we solved the time increments with an explicit forward Euler approach (see Appendix D for details). In a nutshell, given an external force  $\mathbf{f}$  during a small time increment  $\delta t$ , the displacement  $\delta \mathbf{x} = \mathbf{u}$  of a particle on the midplane was found and updated using the following incremental scheme: (a) Assuming a constant distribution tensor  $\boldsymbol{\mu}$ , we used Eq. (5) to find the stresses as a function of  $\mathbf{x}$ . (b) We used this result in Eq. (2) and solved to determine  $\mathbf{u} = \delta \mathbf{x}$ . (c) We then updated the position of the midplane  $\boldsymbol{\varphi}$ , its thickness  $h$ , and all surface properties such as strains and curvatures. (d) We subsequently updated the distribution tensor and chain density following Eqs. (6a) and (6b). (e) Finally, the force  $\mathbf{f}$  was updated, and we started a new time step.

Again, for simplicity, we modeled the VHB tape used in our experiments as a combination of one permanent network (with shear modulus  $G_0$ ) and one dynamic network (with shear modulus  $G_1$  and detachment rate  $k_d$ ). These material parameters were determined by matching model and experimental results as discussed below. For this, we first normalized the

pressure, volume, and inflation rate in the form

$$P^* = \frac{h_0 P}{R(G_1 + G_2)}, \quad V^* = \frac{V}{h_0^3}, \quad W = \frac{\dot{V}}{h_0^3 k_d^0}. \quad (14)$$

The membrane equations were then subjected to fixed volume inflation rates  $W$  for which we predicted the critical volume  $V_c^*$  and pressure  $P_c^*$  [Figs. 5(b) and 5(c)]. As expected, the critical pressure varies between two asymptotes corresponding to the relaxed and instantaneous shear moduli [Fig. 5(b)]. As  $W \rightarrow 0$ , the system behaves elastically and the pressure is equivalent to that obtained with an elastic solution of shear modulus  $G = G_0$ . By contrast, a fast inflation adds a total contribution of  $G_1$  to the shear modulus such that the system has an elastic behavior with instantaneous modulus  $G = G_0 + G_1$ . With this approach, we found that  $G_0 = 23 \pm 3$  MPa [Fig. 5(a)] and  $G_1 = 120 \pm 5$  MPa. We note that the elastic modulus  $G_0$  is on the same order as the value previously found (13.6 kPa) using uniaxial tests [55,56]. At moderate inflation speeds, an appropriate match between the two-network model and experimental curves was difficult to achieve since VHB is known to possess multiple relaxation times [55]. More specifically, experimental curves imply that the relaxation time is stress-dependent, i.e., it flows and relaxes faster under stress. To improve our model, we therefore assumed that the relaxation time  $k_d$  of the dynamic network was an increasing function of the first invariant  $I_1 = \text{tr}(\boldsymbol{\sigma}_{\text{viscous}})$  of the viscous stresses, i.e., the stresses arising from networks 1 to  $N$ . A satisfactory fit for different inflation rates ( $\dot{V} = 0.001\text{--}10$  mL/min) was found when the detachment followed a power law in  $I_1$  of the form  $k_d = 2.7 \times 10^9 (I_1^4)$ . We see in Fig. 5(a) that this model leads to acceptable predictions of the loading stage, the critical pressure, and the initial relaxation times. However, it cannot capture the polymer relaxation at high strains. A more accurate model could be constructed to include the presence of more networks and relaxation times; this is, however, beyond the scope of the present study. Nevertheless, this analysis shows that the conclusions found for the spherical model are still valid for the more complex blister geometry. Note, however, that the relationship between  $W$  and the critical volume and pressure appears shifted to the right in Figs. 5(b) and 5(c). This results from the fact that there is a nonlinear relationship between volume rate  $W$  and strain rate during the inflation process, the former being generally faster than the latter.

### V. CYCLIC LOADING OF A VISCOELASTIC SPHERE

While the study of blister inflation at a fixed rate yielded insightful results regarding its viscous instabilities, many applications seeking to harvest those instabilities occur at loading conditions that are far from constant [57]. Applications of these concepts in reversible actuators [58], soft generators [59], or the control of biofouling [60] are precisely based on the fact that the instability can be cyclically recovered. We therefore propose to explore the mechanisms driving blister relaxation during cyclic inflation and their connection with the buckling phenomenon observed in Sec. II. Motivated by our previous results and other studies [61], we further idealize the blister as a spherical cap, enabling the derivation of exact and insightful analytical solutions.

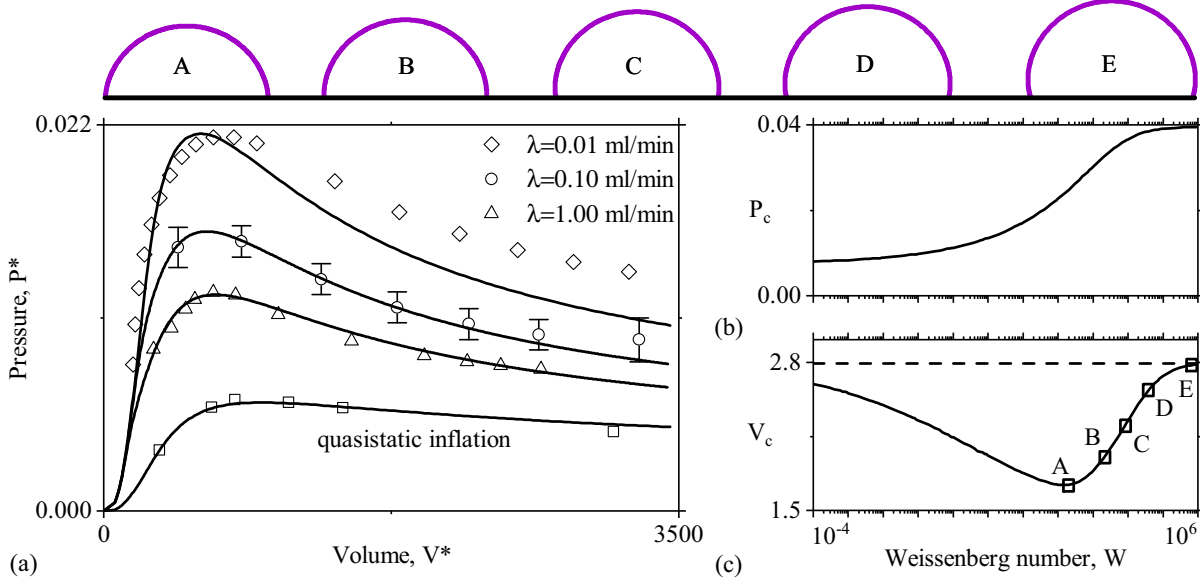


FIG. 5. Normalized pressure  $P^*$  vs the normalized volume of the blister  $V^*$ . The solid lines correspond to our model results while the symbols are experimental data obtained at three different speeds, i.e.,  $V = 0.01$ ,  $0.1$ , and  $1$  mL/min plus an additional set of data obtained using a quasistatic inflation  $V \rightarrow 0$ . (b),(c) Model predictions of the evolution of the critical pressure and volume vs the Weissenberg number. The images on top correspond to the modeled blister profiles at  $P_c - V_c$  for the corresponding Weissenberg numbers indicated in (c).

### A. Step loading

Here, we consider a situation in which the spherical membrane is periodically inflated at a constant rate  $\lambda^*$ , with alternating relaxation periods for a duration  $t_r^* = t_r k_d$  [Fig. 6(a)]. This could correspond, for example, to the evolution of a pathological blister where the incoming volume is periodically interrupted in time. From the previous discussion, it can be inferred that the strain-pressure curve for this situation is bounded by the two elastic solutions corresponding to the relaxed and instantaneous inflation shown in Fig. 6(b). Hence, if the inflation rate is small, one recovers the elastic lower bound, and the solution is independent of time. Similarly, for extremely fast loading ( $\lambda^* \rightarrow \infty$ ) and small relaxation times  $t_r^*$ , one recovers the elastic upper bound. As  $t_r^*$  increases, the stress in the dynamic network relaxes and the pressure

eventually shifts to the elastic lower bound [Fig. 6(b)]. Figure 6(b), however, shows that once the membrane has been allowed to relax multiple times, it converges to the lower bound solution, regardless of the inflation rate.

This observation may be explained as follows: when the dynamic network is allowed to reorganize, its stress-free state corresponds to a larger membrane radius and lower thickness. Since the normalized pressure is scaled with the factor  $h_0/R$  [Eq. (14)], this change in reference reduces the maximum pressure that can be sustained by the dynamic network and shifts the position of the instability. In contrast, the permanent network does not feel any of those changes, and its pressure-strain curve is maintained to the lower bounds. In this situation, for a given membrane stretch  $\lambda_i = 1 + \epsilon_i$ , the corresponding pressure can be split into (a) a pressure  $P_{\text{elastic}}^*$  from the permanent network and (b) a pressure  $P_{\text{viscous}}^*$  from the

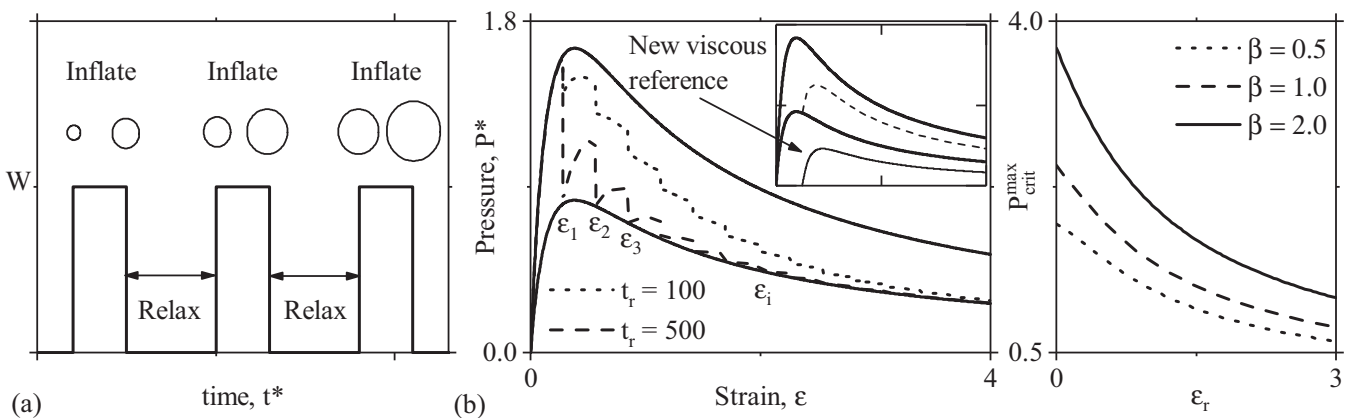


FIG. 6. (a) Weissenberg number variation during a step loading with alternate relaxation times of length  $t_r^*$ . (b) Pressure-strain curves on a spherical shell when the inflation profile of (a) is applied. (c) Variation of the maximum possible pressure on the system with each subsequent, long-lasting pause  $i$  at a strain  $\epsilon_r^i$ .

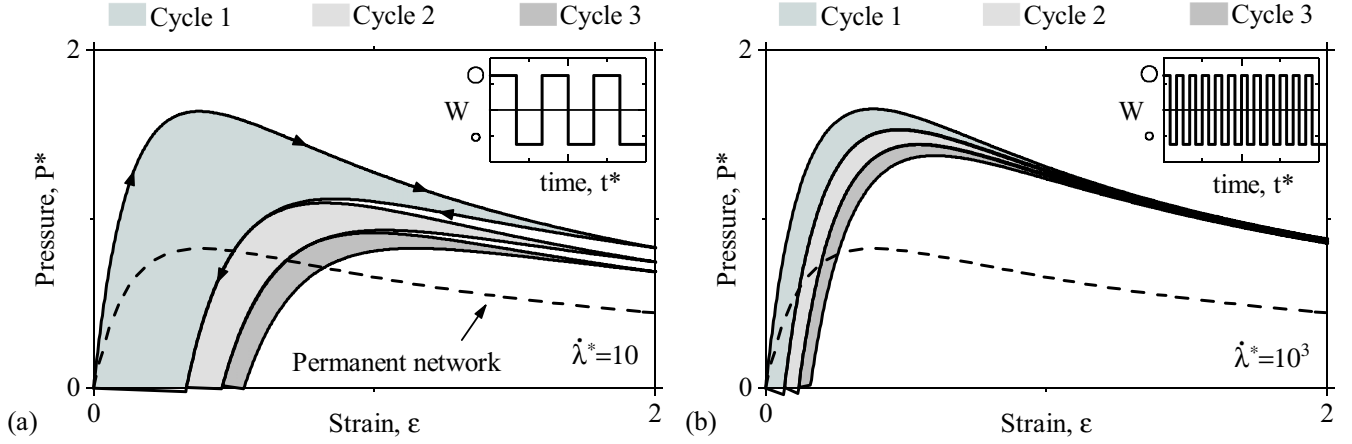


FIG. 7. (a) Pressure-strain curves during the first three cycles of a continuous inflation-deflation process at constant  $|\dot{\lambda}^*| = 10$  on a spherical membrane with  $\beta = 1$ . The colors define the hysteresis produced on each cycle. The dotted line shows the constant contribution of the elastic or permanent network. (b) Same as (a) but using an inflation speed  $|\dot{\lambda}^*| = 10^3$ .

dynamic network resists that progressively relaxes over time. Hence, resuming a fast loading after a long-lasting relaxation at  $\varepsilon_r$  leads to a new maximum pressure-strain relationship of the form

$$P^* = \underbrace{2c_0^* \left( \frac{1}{\lambda} - \frac{1}{\lambda^7} \right)}_{P_{\text{elastic}}^*} + \underbrace{\frac{2c_1^*}{(1 + \varepsilon_i)^3} \left( \frac{1}{\lambda - \varepsilon_i} - \frac{1}{(\lambda - \varepsilon_i)^7} \right)}_{P_{\text{viscous}}^*}. \quad (15)$$

The onset of the instability, which we previously denoted as  $(\lambda_c, P_c)$ , is modified accordingly. As the dynamic network reaches a new stress-free state at higher  $\varepsilon_r$ , the location of the instability is consequently shifted to higher stretch values, and its magnitude is progressively reduced as shown in Fig. 6(c). This decay is even more evident at higher values of  $\beta$ , where the contribution of the viscosity is more prominent. This result implies that the rubber instability normally seen during inflation cannot be recovered for long relaxation periods. To attenuate this effect, one can minimize the total energy lost during relaxation, i.e., having smaller relaxation periods and inflating at higher speed.

### B. Cyclic inflations

Let us finally turn to a scenario during which the membrane follows a periodic inflation-deflation cycle shown in the inset of Fig. 7(a) and that would recapitulate the conditions felt by a soft reversible actuator, for example. More specifically, the membrane is first inflated at a constant rate  $\lambda$ , then kept at constant volume, and finally subjected to a deflation rate  $-\lambda$ , all steps occurring in the same time interval  $t_0^*$ . The predicted pressure response of this system is depicted in Figs. 7(a) and 7(d), depicting three inflation-deflation cycles with a maximum strain  $\varepsilon_{\text{max}} = 2$  at two different rates. We observe that the membrane initially follows a typical pressure-strain curve during inflation, but the same path is not followed during deflation as the system loses energy (hysteresis) due to the viscous effects. The magnitude of this hysteric region is affected by the system dynamics such that it decreases as the

inflation speed becomes larger and it vanishes when  $W \rightarrow \infty$ . This observation has two important outcomes. (a) Since the dynamic network progressively relaxes, recovering the initial condition  $V^* = 0$  induces compressive stresses. Although these stresses would eventually relax, they can result in the temporary buckling of the shell. The onset of buckling ( $P^* = 0$ ) occurs at a larger strain for a slowly inflated membrane and is further increased with each inflation cycle (Fig. 7). This is consistent with the results observed in Fig. 2(b), where the dynamic network in a slowly inflated blister has enough time to relax so that it reaches a larger volume at buckling. By contrast, a quickly inflated blister has less time to relax, which induces the buckling instability at smaller volumes [Fig. 2(b)]. (b) After being cyclically loaded, the rubber instability not only occurs at smaller pressures but is also shifted to a larger critical strain. Indeed, while the permanent network always follows the same (dotted) path, the dynamic network resets its reference state at a higher strain, which affects the location of the instability. As we saw in previous cases, the system is bounded by two elastic solutions corresponding to the only two situations in which the membrane would not buckle: an extremely fast and an extremely slow cycle. To a greater or lesser degree, all intermediate cases imply a buckling phase whose recovery time depends on the polymer dynamics. Eventually, since the contribution of the dynamic network scales with  $h/R$  and it is therefore reduced in time, the behavior of the membrane at large strains converges to the elastic, or relaxed, solution. This behavior is observed in our experiments [Fig. 1(b)] where both buckled blisters eventually recovered their corresponding elastic shape, i.e., a partial sphere and a flat surface. Hence, a system based on this instability would undoubtedly need to account for the viscous effects and either load at a larger speed (reducing the hysteresis) or find a way to quickly reset the dynamic network to its original state.

## VI. CONCLUSION

In summary, this study aimed to shine a light on the interplay between elastic instabilities in elastomeric membranes



and their viscous relaxation over time. For this, we developed a membrane-specific version of the transient network theory [62,63] that makes a connection between the mechanisms of bond exchange between molecular chains and the emerging viscoelastic response of the resulting network [64]. Combining this approach with experimental results on commercial adhesive tape (VHB 4905), we showed that for a viscoelastic membrane, the classical pressure instability may be switched and lessened by changing the inflation rate. We found that the blister displays a rich spectrum of pressure-volume responses that are always bounded by two elastic solutions. In the case of cyclic inflation patterns, viscous relaxation can also trigger membrane buckling, which can potentially be avoided by appropriately tuning the inflation dynamics. On a final note, although blisters are often regarded as a symptom of material pathologies [65], they may be positively harvested during manufacturing processes [66] and actuators. In this context, results from this work may be used to control, fine-tune, and eventually harvest the rubber and buckling instabilities in practical applications. Finally, a fundamental understanding of the interplay between elastic instabilities and viscosity may also be of relevance on a wide variety of synthetic and biological materials, such as non-Newtonian fluids [67], the cell walls of plants and fungi [68], as well as cell sheets [69] and aggregations of insects [70].

#### ACKNOWLEDGMENTS

Research reported in this publication was supported by the National Science Foundation under Award No. 1761918. The content is solely the responsibility of the authors and does not necessarily represent the official views of the National Science Foundation.

#### APPENDIX A: MEMBRANE MECHANICS

From Eq. (1), we can define a local basis on the membrane by defining two tangent vectors to the midplane  $\mathbf{a}_\alpha = \boldsymbol{\varphi}_{,\alpha}$  in addition to a unit normal  $\mathbf{n} = (\mathbf{a}_1 \times \mathbf{a}_2) / \|\mathbf{a}_1 \times \mathbf{a}_2\|$  that determines its orientation (Fig. 3). Hence, a vector and a tensor can be written in the so-called covariant basis  $\{\mathbf{a}_1, \mathbf{a}_2, \mathbf{a}_3\}$  as  $\mathbf{v} = v^i \mathbf{a}_i$  and  $\boldsymbol{\sigma} = \sigma^{ij} \mathbf{a}_i \otimes \mathbf{a}_j$  ( $i, j = 1, 2, 3$ ), respectively. The definition of this basis is completed by defining its metric  $a_{\alpha\beta} = \mathbf{a}_\alpha \cdot \mathbf{a}_\beta$  and curvature  $\kappa_{\alpha\beta} = -\mathbf{a}_\alpha \cdot \mathbf{n}_{,\beta}$  tensors, which are related, respectively, to the change in area and curvature with respect to the parametric space. This basis is, however, not enough to describe all the necessary features to describe a membrane, and we need to define a second (or contravariant) basis  $\{\mathbf{a}^1, \mathbf{a}^2, \mathbf{a}^3\}$  defined by the fact that  $\mathbf{a}^\alpha \cdot \mathbf{a}_\beta = \delta_\beta^\alpha$  (where  $\delta_\beta^\alpha$  is the Dirac delta function) and  $\mathbf{a}^3 = \frac{1}{v} \mathbf{n}$ . In the same way, this basis is characterized by its own metric tensor (with components  $a^{\alpha\beta} = \mathbf{a}^\alpha \cdot \mathbf{a}^\beta$ ) and curvature tensor (with components  $\kappa_\beta^\alpha = -\mathbf{a}^\alpha \cdot \mathbf{n}_{,\beta}$ ) with similar physical meanings. Using these definitions, a vector and a tensor are written, respectively, as  $\mathbf{v} = v^i \mathbf{a}_i$  and  $\boldsymbol{\sigma} = \sigma^{ij} \mathbf{a}_i \otimes \mathbf{a}_j$ . Note that this basis is not necessarily orthonormal, which implies that one must redefine the gradient of a vector and a tensor by taking into account the variation of both the components and the basis. Hence, we can write the divergence and the

gradient as

$$\nabla \cdot \mathbf{v} = (v^i|_i), \quad (\text{A1a})$$

$$\nabla \cdot \boldsymbol{\sigma} = (\sigma^{ij}|_j) \mathbf{a}_i, \quad (\text{A1b})$$

$$\nabla \mathbf{v} = (v^i|_j) (\mathbf{a}_i \otimes \mathbf{a}^j), \quad (\text{A1c})$$

$$\nabla \boldsymbol{\sigma} = (\sigma^{ij}|_k) (\mathbf{a}_i \otimes \mathbf{a}_j \otimes \mathbf{a}^k), \quad (\text{A1d})$$

where the vertical bar indicates a covariant derivative:

$$v^i|_j = v^i_{,j} + \Gamma_{jk}^i v^k, \quad (\text{A2a})$$

$$\sigma^{ij}|_k = \sigma^{ij}_{,k} + \Gamma_{lk}^i \sigma^{lj} + \Gamma_{kl}^j \sigma^{il}, \quad (\text{A2b})$$

and  $\Gamma_{ij}^k = 1/2 a^{il} (a_{jl,k} + a_{kl,j} - a_{jk,l})$  are the Christoffel symbols of the second kind. The comma is used here and in further derivations to indicate derivative with respect to the parametric coordinates, i.e.,  $\partial(\cdot)/\partial \xi^k$ . As discussed in the main text, a thin membrane is described by the expression described in Eq. (1), and thus we can write the velocity of a point located at a parametric position  $\boldsymbol{\xi}$  at a given time  $t$  by

$$\mathbf{v}(\boldsymbol{\xi}, t) = \frac{\delta \mathbf{x}}{\delta t} = v^\alpha \mathbf{a}_\alpha + v^n \mathbf{n} + \xi \dot{\mathbf{a}}_3. \quad (\text{A3})$$

Using this definition, we can obtain the time variation of the local basis by differentiating the surface in both space and time, and considering the fact that  $\partial(\mathbf{a}_\alpha \cdot \mathbf{n})/\partial t = 0$  obtaining

$$\dot{\mathbf{a}}_\beta = (v^\alpha|_\beta - v^n \kappa_\beta^\alpha) \mathbf{a}_\alpha + (v_{,\beta}^n + v^\alpha \kappa_{\alpha\beta}) \mathbf{n}, \quad (\text{A4})$$

$$\dot{\mathbf{a}}_3 = \frac{\dot{h}}{h_0} \mathbf{n} - \frac{h}{h_0} (v^\alpha \kappa_{\alpha\beta} + v_{,\beta}^n) \mathbf{a}^\beta, \quad (\text{A5})$$

and which we can use to derive the velocity gradient. For this, we start by combining these results with Eqs. (A1c) and (A2a) such that we can write the velocity gradient  $\mathbf{L} = \nabla \mathbf{v}$  as

$$\begin{aligned} \mathbf{L} &= (v^\alpha|_\beta - v^n \kappa_\beta^\alpha) (\mathbf{a}_\alpha \otimes \mathbf{a}^\beta) \\ &+ (v^\gamma \kappa_{\gamma\beta} + v_{,\beta}^n) (\mathbf{n} \otimes \mathbf{a}^\beta) \\ &+ \frac{\dot{h}}{h_0} \mathbf{n} \otimes \mathbf{a}^3 - \frac{h}{h_0} (v^\alpha \kappa_{\alpha\beta} + v_{,\beta}^n) \mathbf{a}^\beta \otimes \mathbf{a}^3. \end{aligned} \quad (\text{A6})$$

In parallel, we can also expand the time derivative of the tensor  $\boldsymbol{\mu}$  as

$$\begin{aligned} \dot{\boldsymbol{\mu}} &= \dot{\mu}^{\alpha\beta} \mathbf{a}_\alpha \otimes \mathbf{a}_\beta + \mu^{\alpha\beta} \dot{\mathbf{a}}_\alpha \otimes \mathbf{a}_\beta + \mu^{\alpha\beta} \mathbf{a}_\alpha \otimes \dot{\mathbf{a}}_\beta \\ &+ \dot{\mu}^{33} \mathbf{a}_3 \otimes \mathbf{a}_3 + \mu^{33} \dot{\mathbf{a}}_3 \otimes \mathbf{a}_3 + \mu^{33} \mathbf{a}_3 \otimes \dot{\mathbf{a}}_3, \end{aligned} \quad (\text{A7})$$

and by introducing here Eqs. (A4) and (A6) it is straightforward to see that

$$\dot{\boldsymbol{\mu}} = \dot{\mu}^{\alpha\beta} \mathbf{a}_\alpha \otimes \mathbf{a}_\beta + \dot{\mu}^{33} \mathbf{a}_3 \otimes \mathbf{a}_3 + \mathbf{L}\boldsymbol{\mu} + \boldsymbol{\mu}\mathbf{L}^T. \quad (\text{A8})$$

Finally, using the relationship between the Truesdell rate and the time derivative  $\dot{\boldsymbol{\mu}} = \dot{\boldsymbol{\mu}} + \mathbf{L}\boldsymbol{\mu} + \boldsymbol{\mu}\mathbf{L}^T$  and the fact that  $\dot{\boldsymbol{\mu}} = k_a(C - c)/c\mathbf{I} - k_d\boldsymbol{\mu}$  [36], we can identify terms and obtain the expressions of (9).

#### APPENDIX B: PARTICULAR SOLUTIONS

To derive analytical solutions for the deformation of a viscoelastic material, let us start by defining  $\mathbf{F}$  as the deformation

gradient. Assuming a known expression for this tensor in time, one can integrate the distribution tensor by parts to obtain

$$\boldsymbol{\mu} = e^{-k_d t} \mathbf{F}(t) \mathbf{F}(t)^T + \int_0^t k_d [\mathbf{F}(t) \mathbf{F}^{-1}(\zeta) \mathbf{F}^{-T}(\zeta) \mathbf{F}^T(t)] e^{k_d(\zeta-t)} d\zeta, \quad (\text{B1})$$

which one can use to determine the value of the stress in time. To find the stress on a spherical membrane, we start by considering the deformation gradient for an incompressible sphere of radius  $R = \lambda R_0$  as

$$\mathbf{F} = \begin{bmatrix} \lambda & 0 & 0 \\ 0 & \lambda & 0 \\ 0 & 0 & \frac{1}{\lambda^2} \end{bmatrix}. \quad (\text{B2})$$

Then, in order to generalize this problem into the curvilinear coordinates framework of Sec. III, let us consider the parametrization of a sphere in spherical coordinates such that  $\mathbf{x} = [R \sin \xi^1 \cos \xi^2, R \sin \xi^1 \sin \xi^2, R \cos \xi^1]$ . In this context, it is straightforward to see that the metric and curvature tensor read

$$a_{\alpha\beta} = (\lambda R_0)^2 \begin{bmatrix} 1 & 0 \\ 0 & \sin^2(\xi^1) \end{bmatrix}, \quad \kappa_{\alpha\beta} = -\lambda R_0 \begin{bmatrix} 1 & 0 \\ 0 & \sin(\xi^1)^2 \end{bmatrix}. \quad (\text{B3})$$

Combining these two results with Eq. (B1) and recalling that  $\boldsymbol{\mu} = \mu^{ij} \mathbf{a}_i \otimes \mathbf{a}_j$ , we can write the components of the distribution tensor as

$$\mu^{11} = \frac{1}{R_0^2} \left( e^{-k_d t} + k_d \int_0^t \frac{e^{k_d(\zeta-t)}}{\lambda(\zeta)^2} d\zeta \right), \quad (\text{B4a})$$

$$\mu^{22} = \frac{1}{R_0^2 \cos^2 \theta} \left( e^{-k_d t} + k_d \int_0^t \frac{e^{k_d(\zeta-t)}}{\lambda(\zeta)^2} d\zeta \right), \quad (\text{B4b})$$

$$\mu^t = \frac{1}{\lambda^4} e^{-k_d t} + \frac{k_d}{\lambda^4} \int_0^t \lambda(\zeta)^4 e^{k_d(\zeta-t)} d\zeta, \quad (\text{B4c})$$

and by assuming a system made of a permanent and a viscous network, we can write the average stresses (1) in a rubber balloon as

$$\frac{\sigma^{11}}{k_B T} = \frac{c_1 h}{R_0^2} \left( 1 - \frac{1}{\lambda^6} \right) + c_2 h (\mu^{11} - \mu^t a^{11}), \quad (\text{B5a})$$

$$\frac{\sigma^{22}}{k_B T} = \frac{c_1 h}{R_0^2 \cos^2 \theta} \left( 1 - \frac{1}{\lambda^6} \right) + c_2 h (\mu^{22} - \mu^t a^{22}). \quad (\text{B5b})$$

These stresses can be directly introduced into the second of Eqs. (2), which can be understood as the Laplace law in membranes. By setting  $f_n = -P$  and introducing the curvatures from Eq. (B3), we obtain

$$c_1 \left( \frac{1}{\lambda} - \frac{1}{\lambda^7} \right) + c_2 (\mu^\lambda - \mu^h) = \frac{P R_0}{2 k_B T h_0}, \quad (\text{B6})$$

where

$$\mu^\lambda = \frac{1}{\lambda} e^{-k_d t} + \frac{k_d}{\lambda} \int_0^t \frac{e^{k_d(\zeta-t)}}{\lambda(\zeta)^2} d\zeta, \quad (\text{B7a})$$

$$\mu^h = \frac{1}{\lambda^7} e^{-k_d t} + \frac{k_d}{\lambda^7} \int_0^t \lambda(\zeta)^4 e^{k_d(\zeta-t)} d\zeta. \quad (\text{B7b})$$

### APPENDIX C: AXISYMMETRIC DETAILS

In this Appendix, we carry out the mathematical conditions to obtain the axisymmetric form of the equations to finally obtain the equations in an implementation-ready form. Let us start by introducing the following polar parametrization on the midplane:

$$\boldsymbol{\varphi} = [r(\xi^1) \cos(\xi^2), r(\xi^1) \sin(\xi^2), z(\xi^1)]. \quad (\text{C1})$$

By simply applying the definitions of Sec. III, we can derive the metric and curvature tensors as

$$a_{\alpha\beta} = \begin{bmatrix} r'^2 + z'^2 & 0 \\ 0 & r^2 \end{bmatrix}, \quad \kappa_{\alpha\beta} = \begin{bmatrix} \frac{r''z' + r'z''}{\sqrt{a_{11}}} & 0 \\ 0 & -\frac{r z'}{\sqrt{a_{11}}} \end{bmatrix}, \quad (\text{C2})$$

where we used a prime to indicate a derivative with respect to  $\xi^1$ . In a similar way, the Christoffel symbols can be written as

$$\Gamma_{11}^1 = \frac{r' r'' + z' z''}{a_{11}}, \quad \Gamma_{22}^1 = -\frac{r r'}{a_{11}}, \quad \Gamma_{21}^2 = \frac{r'}{2}, \quad (\text{C3})$$

and thus we can write the membrane equations as

$$\sigma_{,1}^{11} + (2\Gamma_{11}^1 + \Gamma_{21}^2) \sigma^{11} + \Gamma_{22}^1 \sigma^{22} + f^1 = 0, \quad (\text{C4a})$$

$$\sigma^{11} \kappa_{11} + \sigma^{22} \kappa_{22} + f^n = 0, \quad (\text{C4b})$$

which can easily be proven to be equivalent to the common membrane equations shown in p. 34 of Libby and Simmonds with the difference that the real stress in the shell corresponds to  $T^\xi = \sigma^{11} a_{11}$  and  $T^\phi = \sigma^{22} a_{22}$ .

### APPENDIX D: NUMERICAL IMPLEMENTATION

To solve Eq. (2) on an axisymmetric shell, we start by discretizing the parametric domain in  $J$  nodes such that any field is stored in vector form as  $\mathbf{u}^T = [u_1 \cdots u_J]$ . Using the extended particle difference method, we may then interpolate any point of this field and its derivatives as

$$\mathbf{u}(\boldsymbol{\xi}) = \Phi_0 \mathbf{u}^T, \quad \mathbf{u}'(\boldsymbol{\xi}) = \Phi_1 \mathbf{u}^T, \quad \mathbf{u}''(\boldsymbol{\xi}) = \Phi_2 \mathbf{u}^T, \quad (\text{D1})$$

where  $\Phi_0$ ,  $\Phi_1$ , and  $\Phi_2$  are the interpolation matrices as defined in [53,54] and evaluated at the point of interest. Having the problem discretized in this manner, we can then solve the strong form of Eq. (2) to determine the displacement of the membrane given an external pressure  $\mathbf{f}$ . However, since the problem is time-dependent, solving for the final displacement directly is not possible and we used, instead, the following explicit scheme where the problem is solved in small increments of  $\mathbf{f}$  in time:

(i) Assuming a constant distribution tensor  $\boldsymbol{\mu}$ , use Eq. (5) to interpolate the stresses, strains, and other magnitudes as a function of  $\mathbf{x}$ .

(ii) In the context of a Newton-Raphson solver, linearize Eq. (2) as a function of the differential displacement  $\delta \mathbf{U}$  such that we can rewrite the balance of linear momentum as the solution to the following system:

$$\mathbf{R} \delta \mathbf{U} + \mathbf{F} = \mathbf{0},$$

where  $\mathbf{F}$  is the residual of Eq. (2), and  $\mathbf{R}$  is the tangent matrix computed as  $\partial \mathbf{F} / \partial \delta \mathbf{U}$ .

(iii) Solve to determine  $\delta \mathbf{U}$  at every node using a standard Newton-Raphson nonlinear solver.

(iv) Update the position of the midplane  $\varphi$ , its thickness  $h$ , and all surface properties such as strains and curvatures.

(v) Update the distribution tensor and chain density by means of Eqs. (6) and (7).

(vi) Update the external pressure  $f$ , and go back to 1.

- 
- [1] I. Starnberger, D. Preininger, and W. Hödl, *Animal Behav.* **97**, 281 (2014).
- [2] R. F. Shepherd, F. Ilievski, W. Choi, S. A. Morin, A. A. Stokes, A. D. Mazzeo, X. Chen, M. Wang, and G. M. Whitesides, *Proc. Natl. Acad. Sci. (USA)* **108**, 20400 (2011).
- [3] S. Emmanuel, J. Bico, E. Reyssat, and B. Roman, in *APS March Meeting* (APS, 2017), p. H18.009.
- [4] G. Salbreux and F. Jülicher, *Phys. Rev. E* **96**, 032404 (2017).
- [5] R. Mangan and M. Destrade, *Int. J. Non-Lin. Mech.* **68**, 52 (2015).
- [6] T. Li, C. Keplinger, R. Baumgartner, S. Bauer, W. Yang, and Z. Suo, *J. Mech. Phys. Solids* **61**, 611 (2013).
- [7] S. Srinivasan, Z. Wei, and L. Mahadevan, *Phys. Rev. Fluids* **2**, 074103 (2017).
- [8] G. T. Charras, M. Coughlin, T. J. Mitchison, and L. Mahadevan, *Biophys. J.* **94**, 1836 (2008).
- [9] E. Benet and F. J. Vernerey, *Phys. Rev. E* **94**, 062613 (2016).
- [10] E. Benet, G. Lostec, J. Pellegrino, and F. Vernerey, *Phys. Rev. E* **97**, 042607 (2018).
- [11] J. C. Weaver and Y. A. Chizmadzhev, *Bioelectrochem. Bioenerg.* **41**, 135 (1996).
- [12] A. Wingert, M. D. Lichter, and S. Dubowsky, *IEEE/ASME Trans. Mechatron.* **11**, 448 (2006).
- [13] J. Zhu, M. Kolloosche, T. Lu, G. Kofod, and Z. Suo, *Soft Matter* **8**, 8840 (2012).
- [14] F. Carpi, B. Siegfried, and D. De Rossi, *Science* **330**, 1759 (2010).
- [15] H. S. Park and T. D. Nguyen, *Soft Matter* **9**, 1031 (2013).
- [16] S. Wang, M. Decker, D. L. Henann, and S. A. Chester, *J. Mech. Phys. Solids* **95**, 213 (2016).
- [17] D. Eder-Goy, Y. Zhao, and B. X. Xu, *Acta Mech.* **228**, 4293 (2017).
- [18] N. M. Ribe, *J. Fluid Mech.* **457**, 255 (2002).
- [19] N. M. Ribe, *Phys. Rev. E* **68**, 036305 (2003).
- [20] E. A. Evans and R. M. Hochmuth, *Biophys. J.* **16**, 1 (1976).
- [21] M. Arroyo and A. DeSimone, *Phys. Rev. E* **79**, 031915 (2009).
- [22] F. J. Vernerey and M. Farsad, *Comput. Methods Biomech. Biomed. Eng.* **14**, 433 (2011).
- [23] L. Foucard, X. Espinet, E. Benet, and F. J. Vernerey, in *Multiscale Simulations and Mechanics of Biological Materials*, edited by S. Li and D. Qian (John Wiley & Sons, Ltd., 2013), Chap. 13, pp. 241–265.
- [24] M. Rahimi, A. Desimone, and M. Arroyo, *Soft Matter* **9**, 11033 (2013).
- [25] R. Okamoto, Y. Kanemori, S. Komura, and J. B. Fournier, *Eur. Phys. J. E* **39**, 52 (2016).
- [26] H. Turlier, B. Audoly, J. Prost, and J. F. Joanny, *Biophys. J.* **106**, 114 (2014).
- [27] A. P. Selvadurai and Q. Yu, *Proc. R. Soc. A* **462**, 189 (2006).
- [28] H. Wang, M. Lei, and S. Cai, *J. Appl. Phys.* **113**, 213508 (2013).
- [29] A. Wineman, *Comput. Math. Appl.* **53**, 168 (2007).
- [30] E. Verron, G. Marckmann, and B. Peseux, *Int. J. Numer. Methods Eng.* **50**, 1233 (2001).
- [31] F. Erchiqui, A. Gakwaya, and M. Rachik, *Polym. Eng. Sci.* **45**, 125 (2005).
- [32] E. Verron, R. Khayat, A. Derdouri, and B. Peseux, *J. Rheol.* **43**, 1083 (1999).
- [33] A. D. Drozdov, *Acta Mech.* **133**, 13 (1999).
- [34] J. Zhang, H. Chen, and D. Li, *J. Appl. Phys.* **123**, 084901 (2018).
- [35] F. Tanaka and S. F. Edwards, *Macromolecules* **25**, 1516 (1992).
- [36] F. J. Vernerey, R. Long, and R. Brighenti, *J. Mech. Phys. Solids* **107**, 1 (2017).
- [37] M. S. Green and A. V. Tobolsky, *J. Chem. Phys.* **14**, 80 (1946).
- [38] M. Rahimi and M. Arroyo, *Phys. Rev. E* **86**, 011932 (2012).
- [39] S. Q. Wang, *Macromolecules* **25**, 7003 (1992).
- [40] S. A. Langer and U. Seifert, *Europhys. Lett.* **23**, 71 (1993).
- [41] C. Perdigou and B. Audoly, *J. Mech. Phys. Solids* **96**, 291 (2016).
- [42] C. Keplinger, M. Kaltenbrunner, N. Arnold, and S. Bauer, *Proc. Natl. Acad. Sci. (USA)* **107**, 4505 (2010).
- [43] J. Zhang, J. Ru, H. Chen, D. Li, and J. Lu, *Appl. Phys. Lett.* **110**, 044104 (2017).
- [44] J. Simo and D. Fox, *Comput. Methods Appl. Mech. Eng.* **72**, 267 (1989).
- [45] A. E. Green and W. Zerna, *Theoretical Elasticity* (Oxford University Press, London, 1968), p. 457.
- [46] H. Watanabe, *Prog. Polym. Sci. (Oxford)* **24**, 1253 (1999).
- [47] T. F. A. de Greef and E. W. Meijer, *Nature (London)* **453**, 171 (2008).
- [48] L. Leibler, M. Rubinstein, and R. H. Colby, *Macromolecules* **24**, 4701 (1991).
- [49] F. J. Vernerey, *J. Mech. Phys. Solids* **115**, 230 (2018).
- [50] J. A. Rodríguez-Martínez, J. Fernández-Sáez, and R. Zaera, *Int. J. Eng. Sci.* **93**, 31 (2015).
- [51] E. Verron and G. Marckmann, *Int. J. Non-Lin. Mech.* **38**, 1221 (2003).
- [52] A. Libai and J. G. Simmonds, *The Nonlinear Theory of Elastic Shells*, 2nd ed. (Cambridge University Press, New York, MA, 1998).
- [53] Y.-C. Yoon and J.-H. Song, *Comput. Mech.* **53**, 1087 (2014).
- [54] Y. C. Yoon and J. H. Song, *Comput. Mech.* **53**, 1105 (2014).
- [55] M. Hossain, D. K. Vu, and P. Steinmann, *Comput. Mater. Sci.* **59**, 65 (2012).
- [56] T. Lu, J. Huang, C. Jordi, G. Kovacs, R. Huang, D. R. Clarke, and Z. Suo, *Soft Matter* **8**, 6167 (2012).
- [57] F. Chen, J. Zhu, and M. Y. Wang, *EPL* **112**, 47003 (2015).
- [58] L. Hines, K. Petersen, and M. Sitti, *Adv. Mater.* **28**, 3690 (2016).
- [59] T. G. McKay, B. M. O'Brien, E. P. Calius, and I. A. Anderson, *Appl. Phys. Lett.* **98**, 142903 (2011).
- [60] X. Zhao and Q. Wang, *Appl. Phys. Rev.* **1**, 021304 (2014).
- [61] R. Long, K. R. Shull, and C. Y. Hui, *J. Mech. Phys. Solids* **58**, 1225 (2010).

- [62] S. L. Sridhar and F. J. Vernerey, *Polymers* **10**, 848 (2018).
- [63] R. Brighenti, F. Artoni, F. Vernerey, M. Torelli, A. Pedrini, I. Domenichelli, and E. Dalcanale, *J. Mech. Phys. Solids* **113**, 65 (2018).
- [64] F. J. Vernerey, R. Brighenti, R. Long, and T. Shen, *Macromolecules* **51**, 6609 (2018).
- [65] K. T. Wan and Y. W. Mai, *Acta Metall. Mater.* **43**, 4109 (1995).
- [66] J. M. Charrier, S. Shrivastava, and R. Wu, *J. Strain Anal.* **24**, 55 (1989).
- [67] V. Barra, S. A. Chester, and S. Afkhami, *Comput. Fluids Computers and Fluids* **175**, 36 (2018).
- [68] S. L. Sridhar, J. K. E. Ortega, and F. J. Vernerey, *Biophys. J.* **115**, 2428 (2018).
- [69] S. Ishihara, P. Marcq, and K. Sugimura, *Phys. Rev. E* **96**, 022418 (2017).
- [70] F. J. Vernerey, T. Shen, S. L. Sridhar, and R. J. Wagner, *J. R. Soc. Interface* **15**, 20180642 (2018).